

# Characterization of major discontinuities from borehole cores of the black consolidated marl formation of Draix (French Alps)

A. Neuville<sup>1,2</sup>    R. Toussaint<sup>1,2</sup>    J. Schmittbuhl<sup>1,2</sup>  
D. Koehn<sup>3</sup>    J.-O. Schwarz<sup>3</sup>

March 23, 2010

amelie.neuville@eost.u-strasbg.fr  
renaud.toussaint@eost.u-strasbg.fr  
jean.schmittbuhl@eost.u-strasbg.fr  
koehn@uni-mainz.de

Submitted to HP - special issue paper, with the reference S147 Clay Shales and Clayey Sediments

## Abstract

A quantitative description of rock discontinuities present in subsurface cores that were drilled (down to 20 m) in the marls of the Laval and Moulin catchments near Draix (France) is presented. Three kinds of discontinuities are studied: those fully open, those open but filled with clay rich material and those sealed with calcite. With a laser profiler, the topography of facing sides of typical discontinuities was measured with a normal resolution of 1  $\mu\text{m}$ . The probability distribution of the elevation of each surface are obtained and shown to be normal. Possible self-affine scaling invariance of the topography were explored. The mineralogical content of an interface between the marl bulk and the embedded calcite vein is also investigated using X-ray

---

<sup>1</sup>EOST, Université de Strasbourg, France

<sup>2</sup>Institut de Physique du Globe de Strasbourg, UMR CNRS Uds 7516, 5 rue René Descartes, 67087 Strasbourg Cedex, France

<sup>3</sup>Johannes Gutenberg Universität Mainz, Institut für Geowissenschaften , Becherweg 21, 55099 Mainz, Germany

computed tomography. Implication of this study for water transport in such discontinuities are addressed in a companion paper in the same issue.

## 1 Introduction

In catchments like the Laval and Moulin ones, located near Draix, in the South French Alps mass movements frequently occur in the black consolidated marl formation (“Terres Noires”) (Fressard et al., 2009). The landslides are often due to water driven processes. Indeed, water causes a chemo-mechanical weathering of the rock, which modifies the geometry of the subsoil and the mechanical stability of the rocks and slopes. For a given solid stress along an interface prone to sliding, the decrease of effective pressure leads to an increase of the ratio of tangential stress over effective pressure, bringing this ratio closer to a Coulomb sliding threshold, which increases the slope failure potential (Terzaghi, 1936; Iverson and Reid, 1992). High pore pressure may also trigger hydraulic fracturing which can increase the size of the fractures and enhance downslope movements of blocks along the fractures. If water does not seep into the bedrock, it may trigger debris flows (Yamakoshi et al., 2009) and important surface runoffs which carry a significant amount of material (e.g. Antoine et al. (1995); Mathys (2006)).

In order to understand the Draix landslides, five boreholes were drilled at the top of a stable interfluvium, between the Laval and Moulin catchments (Fig. 1). Among them is the borehole SC1 which was completely cored showing numerous major discontinuities. Hydraulic studies in the surrounding area (Cosandey et al., 2007) and studies where tracer tests between these boreholes are performed (Garel et al., 2009; Lofi et al., 2009) show that the fractured marl has a significant role in the hydraulic balance. At field scale, mass losses of water complicates the permeability estimation of the fractured bedrock. At core scale, hydraulic tests are also difficult to perform as the permeability is due to large discontinuities intercepting the core while the rock matrix (marl) has a negligible permeability.

The permeability of each main discontinuity of the Draix fractured bedrock is probably highly influenced by their precise geometry as the hydraulic behavior of rough open fractures is significantly affected by the fracture roughness (e.g. Brown (1987); Glover et al. (1997); Méheust and Schmittbuhl (2000, 2003); Plouraboué et al. (2000); Drazer and Kopolik (2002); Auradou et al. (2005); Barton et al. (1997)). This was also shown by studies about fracture morphology that were carried out in parallel with experiments aiming at measuring their hydraulic behavior (e.g. Vicente Silvestre et al. (2002); Hakami and Larsson (1996)).

The present paper focuses on how to measure and characterize the topography of the surfaces of typical discontinuities sampled during coring. The knowledge of the fracture side topography is a first step towards a description of the hydraulic behavior of the Draix formation, which is done in a companion paper in the same issue (Neuville et al., 2009), hereafter referred as paper 2.

This article is organized as follows: in section 2, a description of the drilling procedure is given, as well as the definition of morphological units of the core. The location of the four studied discontinuities is also presented. These discontinuities are described in a qualitative way in section 3. Section 4 shows the topography measurements that have been performed on the facing surfaces of each discontinuities using a laser profiler. An X-ray computer tomography has also been used to image the mineralogical content of an interface between marl and an embedded calcite vein. In section 5, a statistical study of the topography fluctuations is presented.

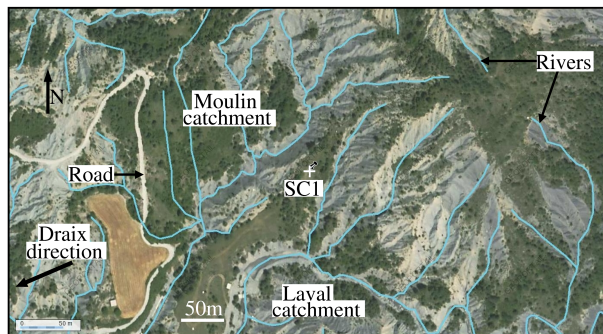


Figure 1: Aerial photography and river locations, modified after [www.geoportail.fr](http://www.geoportail.fr) (Geoportail, 2009), showing the surroundings of the well SC1 (indicated by the label SC1, located at longitude  $06^{\circ}21'43''\text{E}$  and latitude  $44^{\circ}08'30''\text{N}$  in the WGS84 standard). The surrounding catchments are the Laval and Moulin ones. The nearest town is Draix, located at 1.6 km south-east from the well SC1.

## 2 Core log description and localization of the studied discontinuities

The studied discontinuities come from a coring of 10 cm in diameter, extracted from the SC1 borehole (20 m deep) and located between the Laval and Moulin catchments near Draix, French Alps (Fig. 1). One should keep in mind that the sample collected from the well might not be fully representative of the whole bedrock as it is only a local sampling. Due to the

heterogeneity of the subsoil and stress field, local open discontinuities exist, the stress being then transmitted through the contact zones of the discontinuities. Studying the discontinuities requires the cores to be recovered as intact as possible, which was possible owing to special care during SC1 drilling. More specifically, a triple tube core barrel was used, which consists in two embedded external metallic tubes and an internal transparent plastic tube. In this system, only the external metallic tube rotates while both inner tubes are fixed, so that there is little rotation or vibration of the core (Wyllie, 1999). The core was directly stored in the inner plastic tube, so that most of the infill and fractured parts was recovered (excepted maybe at the end and beginning of each core). Plastic tubes were then quickly sealed so that the moisture content was kept, preventing the dessication of the marl during the storage time. Moreover, the second metallic tube also prevents the core from being damaged by the drilling fluid (here: water). As the cores were studied at ambient air and because of core handling, crumbled marl or clayey infill might have been damaged. The study of the surface was therefore performed only on parts of the core fairly resistant to dessication and manipulations. In any case, the coring does not modify sealed discontinuities that will also be of interest for the morphology characterization.

From cores and well logs (Lofi et al., 2009), the local stratigraphy is divided into three major units (Fig. 2a) (Bondabou, 2007; Mery, 2008). Below 6.3 m, the core consists of a consolidated matrix intercepted by large discontinuities and altered zones. The matrix is a compact black marl which was described as resistant, structured, and cohesive by Maquaire et al. (2002). The consolidated part of the core is divided into two units: the lowest is unit 1 (see Fig. 2a) which shows numerous sealed veins, filled with recrystallized calcite, probably issued from water flow from surrounding zones richer in carbonates (Cras, 2005; Bondabou, 2007). Lying above unit 1 is unit 2 which is intercepted by open fractures and discontinuities filled with clayey materials. Above 6.3 m the cores are less consolidated. Just above the consolidated marls lays a transition zone, unit 3b, with highly altered marl. The top part of the core is unit 3 which consists of unconsolidated layers with soft clay and limon.

In unit 2, two discontinuities (F9 and F6) respectively located at depths 9.3 m and 6.6 m are studied (Fig. 2). The discontinuity F9 is open while F6 is filled with debris and clay. In unit 3, a sample (C14) consisting mainly of calcite, located in an altered zone, at 14.6 m depth is also studied, as well as a sample (C12) consisting of two very thin calcite veins embedded into the marl, located around 12 m depth. Samples C10 and C17 are other examples of calcite veins.

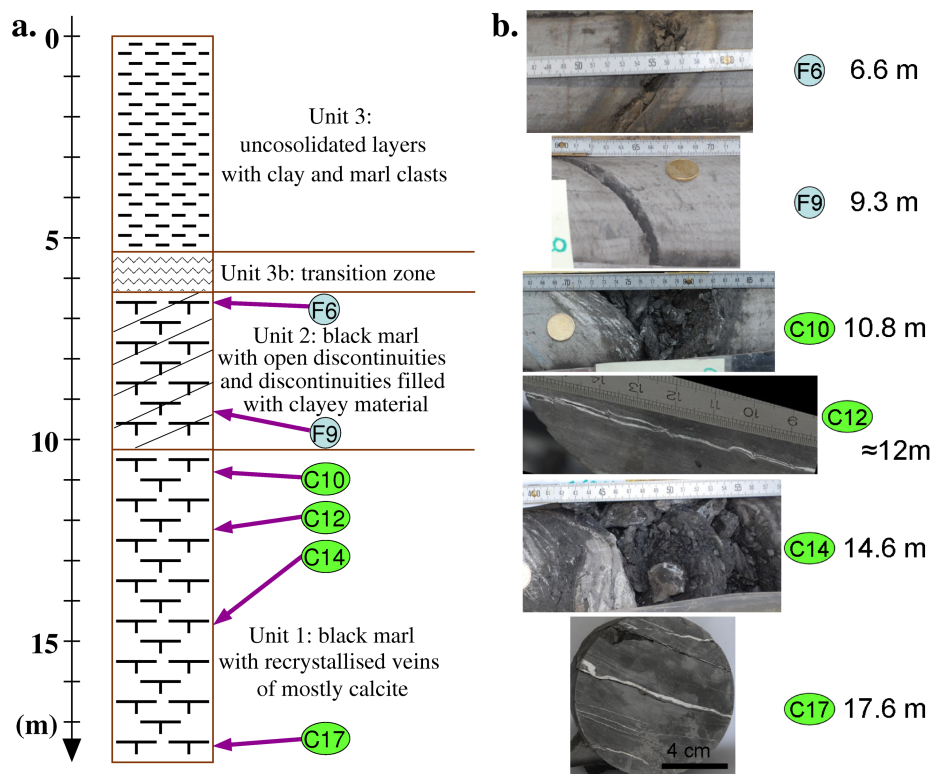


Figure 2: a. Stratigraphic log after the indications of J. Ortega and J.-P. Malet. b. Picture of typical discontinuities with depth. Scale on the pictures is given by the ruler in cm.

### 3 Qualitative description of the discontinuities

#### 3.1 Description of the open discontinuity

F9 is an open discontinuity located inside a compact dark gray marl which follows approximately the schistosity with an apparent dip of 42 degrees with respect to the plane perpendicular to the core direction, i.e. roughly the horizontal plane (angle measured on the sample with an inclinometer, with a precision of  $\pm 0.5$  degrees). The discontinuity F9 looks scarcely altered (Fig. 2) with many complementary reliefs appearing on both surfaces once one of the surfaces is translated. Facing oxidized zones on both sides (Fig. 3a) are signs of water circulation. The presence of these oxides shows that this discontinuity existed before the borehole was drilled.

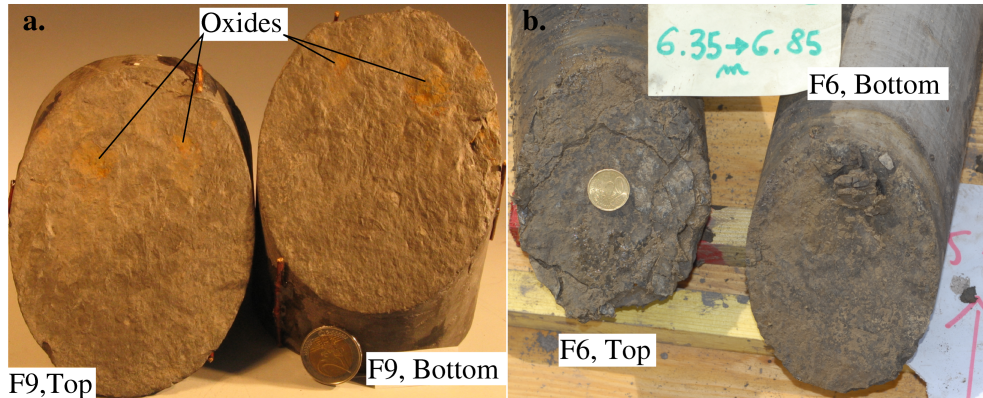


Figure 3: a. Facing surfaces of the discontinuity F9. Oxidized zones can be observed on both faces. b. Facing surfaces of the discontinuity F6, covered with a layer of clay. This layer was removed before studying the topography of the surfaces.

### 3.2 Description of the discontinuity filled with debris and clay

The second discontinuity studied in unit 2 is the discontinuity F6, which is also located in a compact dark gray marl, following approximately the schistosity. Contrary to F9, F6 shows clear signs of degradation (see Fig. 3b). F6 is surrounded with a layer of marl which is oxidized (darker region on Fig. 2b). This discontinuity was filled with clay and marl fragments which are presumably coming from a local water circulation (Cras, 2005; Bondabou, 2007). When observing the discontinuity F6 just after it was taken out of the plastic tube, it was seen that both sides were covered with a 2 mm thick clay layer (Fig. 3b). The morphology and composition of such a layer is definitively very sensitive to any in situ water content or flow change. As our study stands at ambient air, this layer would have been modified by dessiccation. Consequently, we chose to study the topography of the competent rock surface, which appeared once the clay layer had been washed out.

### 3.3 Description of sealed discontinuities

Several veins filled with calcite intersect the cores, in particular in unit 1 (Fig. 2). The thickness of the calcite joints ranges from less than 0.1 mm to about 15 mm. A simple case would be that the discontinuity consists in a single fracture filled with calcite. In that case, assuming the morphology to remain constant during the calcite crystallization, the calcite vein would be a direct cast of the fracture aperture. However, observing the content of these

sealed zones excludes this hypothesis: indeed they seem to be formed during a series of crystallization episodes. Complex zones that consist of several anastomosed parallel calcite veins are frequent in unit 1 (e.g. zones C10, C12, and C14 in Fig. 2b); individual calcite veins are therefore hardly visible. Parallel fractures, either open or sealed, located in C17 sample (Fig. 2b), suggest that the calcite vein concentrates stresses in the vicinity of the vein in the embedding rock, provoking new fractures along the interface, which will be filled at a later time. Therefore these sealed zones, which seem to have formed during several opening/crystallization episodes, are too complex to be seen as casts of single pre-existing fractures. However, independently from the formation scenario, each complex zone could become a single open transport zone, if the calcite is later dissolved.

In particular, two zones, C14 and C12 (Figs. 2 and 4), which are located in unit 1, are studied. The calcite discontinuity, C14, is studied by laser profilometry on both sides. As C14 is a core fragment detached from the consolidated part of the core, the orientation of the joint in the core is not known. Therefore the sides are arbitrarily assigned as bottom and top. In addition, to understand the connection between the calcite content and the in-situ interface between the sealed discontinuity and the surrounding marl, an X-ray computed tomography was performed on a similar calcite vein, C12.



Figure 4: Profile picture of the calcite vein, C14, located at 14 m depth near the complex zone shown in Fig. 2b. The picture shows the typical thickness of the calcite vein and the complexity of the sample because of multi-layer structure.

## 4 Measurement of the morphology of the discontinuity sides

### 4.1 Laser profiler measurement of the surfaces

The topography of surface pairs of the discontinuities F6, F9, and C14 was obtained (Figs. 6, 7, 8) using a laser profiler (Méheust, 2002; Schmittbuhl et al., 2008). The instrument (Fig. 5a) sends a vertical laser beam (diameter 30  $\mu\text{m}$ ) towards the surface. If the surface is diffusive enough, the two

charge-coupled devices (CCD) located on each side of the laser head are able to register the position of the diffusion spot on the surface. A calibration procedure, which is carried out before each measurement, provides a measure of the distance between the laser head and the reflecting surface with a precision of  $1\ \mu\text{m}$ . The measurement is carried on-the-flight, while the laser head moves along a regular planar array above the scanned surface. The grid mesh size of the measured topography of F9 and F6 sides is  $40\pm 2\ \mu\text{m} \times 40\pm 0.1\ \mu\text{m}$  in the horizontal plane and the vertical precision of the measured topography is about  $1\ \mu\text{m}$ . However, to reduce computer time, in this study, the horizontal plane resolution is reduced for F6 by a cubic interpolation to a mesh of  $200\ \mu\text{m} \times 200\ \mu\text{m}$ . The morphology of the surfaces of the calcite vein C14 was also measured with the profiler (Fig. 5b) with an in-plane resolution of  $150\ \mu\text{m} \times 150\ \mu\text{m}$ .

When doing the topography measurement of the F9 and F6 surfaces, each surface was fixed approximately horizontally. After the surface measurement was finished, a mean plane was fitted by a least mean square method on a relevant subset (i.e. without taking into account notches or outliers) of the measured surface. A rotation of the axes is then performed to get the so called  $x - y$  plane aligned with the mean plane of the surface. A translation along the  $z$ -axis is also applied relevant so that the average of the height values is equal to  $\langle h \rangle = 0$ . In Figs. 6, 7 and 8, the  $x$  and  $y$  axes define the mean plane of the surface, the  $z$ -axis being perpendicular.

For the open discontinuities, like F6 or F9, the top and bottom surfaces which are studied are located on two different parts of core, whose relative position is a priori lost. On the contrary, for the sealed discontinuity C14, the topography of each side of a single rock piece has to be measured. Therefore, if, when doing the topography measurements, there exists a rigid reference frame common for both sides, one can infer their relative position (see paper 2). To this aim, sample C14 was docked within a rigid box, as shown in Fig. 5b.

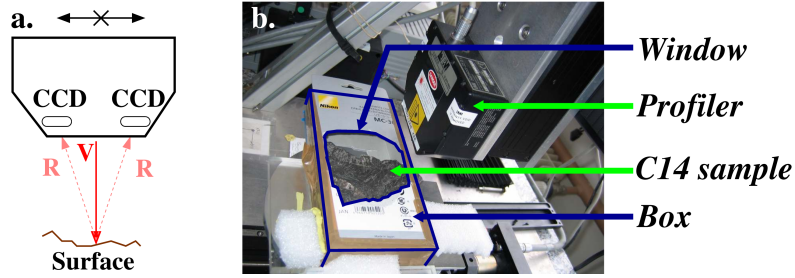


Figure 5: a. Schematic diagram of the optical profiler. The letter 'V' stands for the vertical beam, and 'R' for the light reflected towards the CCD. b. Measurement of calcite vein C14 with laser profiler. The sample is wedged in a box where two windows allow to see the top and bottom sides of the sample. The box is used as benchmark to know the relative position of both sample sides, which is useful for further analyzes.

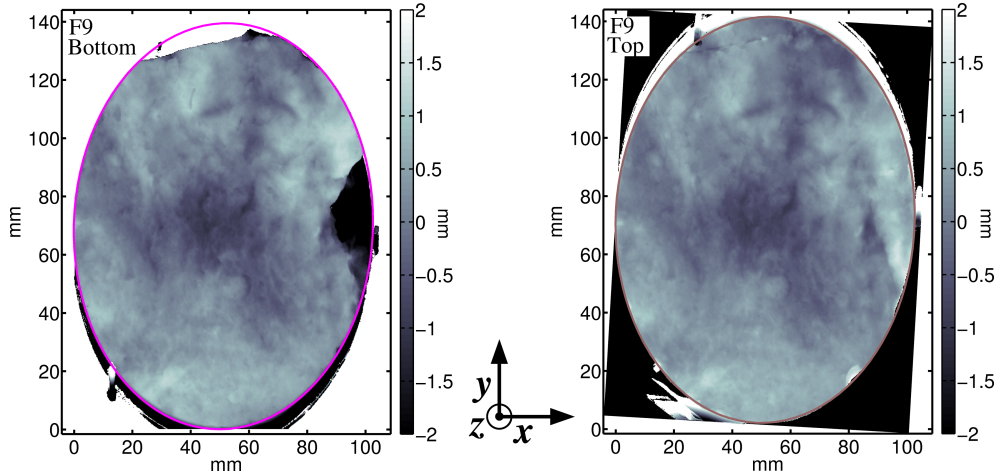


Figure 6: Topography of both facing F9 surfaces, measured by the laboratory profiler and shown once the axes are rotated and shifted so that the mean plane (obtained by a least mean square method) of the surface corresponds to the  $x - y$  plane. The top surface (on the right) is presented after rotation of  $180^\circ$  around the  $y$ -axis, in order to stress the similarity between top and bottom surfaces. A rotation of  $3.3^\circ$  around the  $z$ -axis was also performed in order to maximize the correspondence between similar patterns of the top and bottom surfaces. On both figures the complementary asperities are therefore located at the same coordinates, and because of the rotation around the  $y$ -axis, they are shown with the same level of gray. Elliptic fits of the core boundary are also plotted for both surfaces (same ellipse size for both cores).

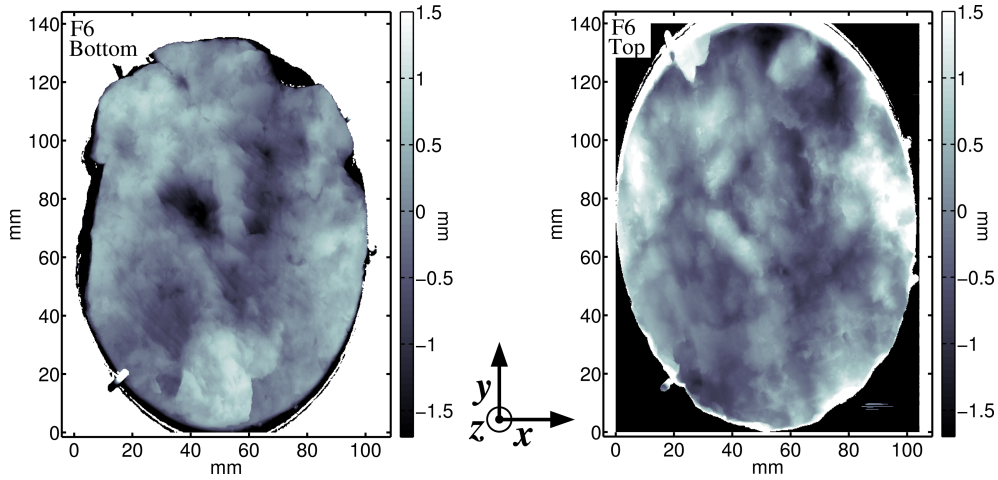


Figure 7: Topography (measured by the laser profiler) of both facing F6 surfaces, presented after treatments similar to those applied to F9 in Fig. 6. Here no clear correlation between the two sides is visible.

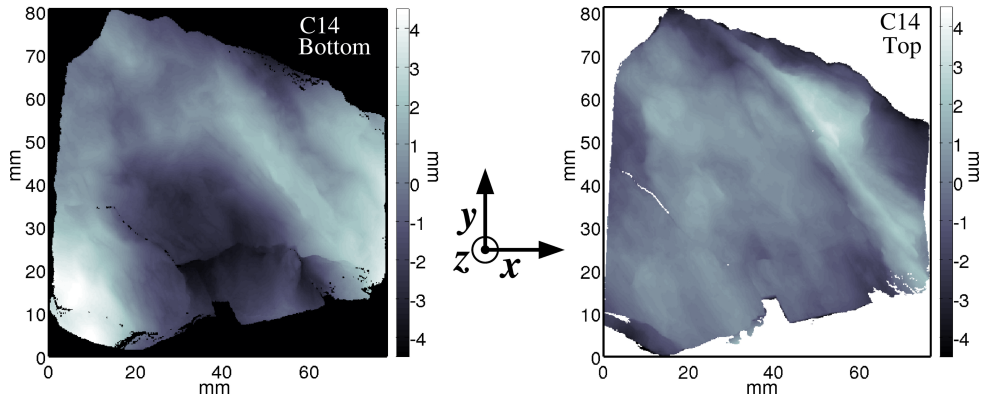


Figure 8: Topography of the external sides of the calcite vein C14, measured by the laser profiler, shown after each trend of the surfaces was removed. The top surface is presented after rotation of  $180^\circ$  around the  $y$ -axis, in order to see the similarities between top and bottom surfaces.

## 4.2 Detailed study of the interface between calcite sealed discontinuities and the marl bulk using X-ray computed tomography

Observing sample C14, (Fig. 4), it was noticed that the interface between calcite and marl was not a clear boundary but rather a zone of alternating

calcite and black marl layers, each being thinner than 0.5 mm. To check the volumetric structure of the transition from the vein to the surrounding embedding marl, the sample C12, which contains two very thin calcite layer ( $\leq 1$  mm), was investigated by X-ray computed tomography (CT).

Figure 9a shows an example of a bidimensional (2D) slide extracted from the tridimensional (3D) measurement (axes  $x - y - z$  provided by the CT device). The X-rays transmitted by the material are sensitive to the local density (e.g. see references related to tomography principle in Zhang et al. (2004)): the dark parts of Fig. 9a correspond to low density areas. The calcite, whose density is  $2.7 \cdot 10^3$  kg/m<sup>3</sup>, looks brighter than the dry marl, which has a density of about  $2.3 \cdot 10^3$  kg/m<sup>3</sup> (Carmichael, 1990). For this measurement, the calcite layers were approximately oriented along the  $z$ -axis. The resolution is given by isotropic grid meshes of  $90.2 \times 90.2 \times 90.2$   $\mu\text{m}^3$ .

A density evolution was observed in the direction approximatively perpendicular to the calcite vein, i.e. along  $x$ -profiles (Fig. 9b). As the calcite infill is not a perfect plane, the beginning of each  $x$ -profiles was adjusted so that  $x = 0$  when the density is below 3% of the calcite density. Figure 9b shows the variability of such density profiles. Density profiles were then averaged, over a set of  $18 \times 70$  profiles, respectively for the  $z$  and  $y$  axes, separated by steps of 4.5 mm along  $z$  and 90.2  $\mu\text{m}$  along  $y$  (Fig. 10). The calcite density in dimensionless units is about 1 while the marl density is about 0.8. Figure 10 shows that the transition from a zone rich in calcite to a zone poor in calcite occurs in two steps: a very sharp evolution over roughly 0.15 mm (less than two grid meshes), and a smoother evolution over several mm. The zone rich in calcite probably results from precipitation of water rich in carbonates into an open discontinuity. The other zone would corresponds to a zone with mostly marl and little calcite, which could come from precipitation of water rich in carbonates after the water has diffused into the porosity of the marl bulk.

With a higher resolution, it would be interesting to use these profiles, select a given threshold and determine the topography of the interface at this threshold (see for instance Noiriel (2005)). As we observed that this vein could not be easily separated from the surrounding marl – certainly due to the calcite content in the marl and the absence of a sharp transition in calcite content –, it was then not possible to perform a compared study of such surface determined by density thresholding, and the same one measured by laser profilometry.

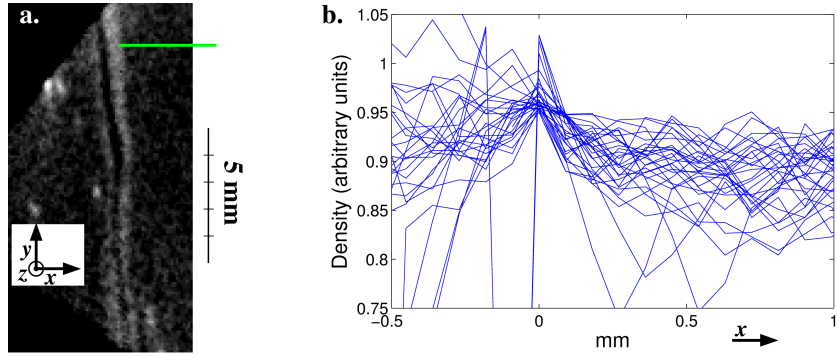


Figure 9: a. Slide obtained from 3D X-ray computed tomography of the calcite veins contained in C12 (Fig. 2b). The calcite veins are approximately parallel to the  $z$ -axis. The thickness of these veins is less than 1 mm. The line shows an example of an  $x$ -profile along which the density was studied. b. 70 density profiles oriented along the  $x$ -axis, perpendicularly to the approximate mean plane of the calcite vein embedded in C12, showing the variability of the density. For all these profiles, the  $x$ -axis is shifted so that  $x=0$  corresponds to a density below 3% of the density of the calcite. The density is normalized by the calcite density.

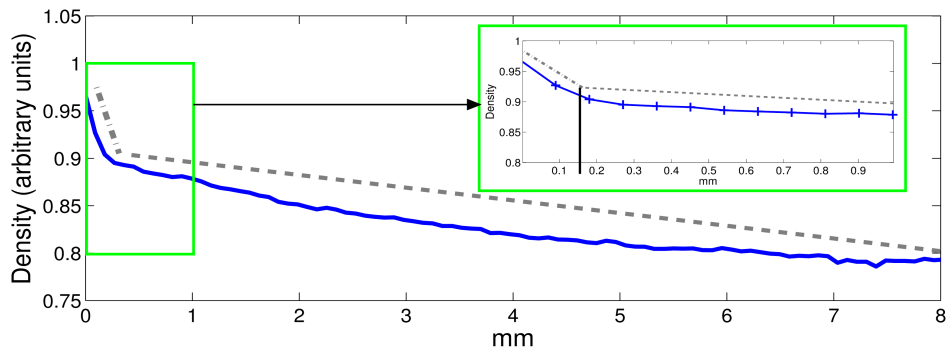


Figure 10: The density profile shown is the average of 1260 profiles similar to the ones shown in Fig. 9b, taken across the whole surface of the calcite vein, distributed over a surface about  $6 \times 70 \text{ mm}^2$ . Two density gradients, underlined by the dotted lines, are observed at the transit from the calcite density to the marl density: a sharp transition, extending over 0.15 mm, (see blow up), and a smoother one, extending over several mm.

## 5 Statistical characterization of the roughness of the discontinuity surfaces

A statistical study along the topography variations of the discontinuity sides is presented here. The goal is to obtain a geometrical model of the asperities in terms of magnitude, density and spatial correlations that could possibly be extended at larger scales.

### 5.1 Statistical characterization of F9 discontinuity sides

As seen on the probability distribution function shown in Fig. 11a, computed for F9, the elevation of both discontinuity sides follows a normal distribution having a standard deviation of  $0.4 \pm 0.05$  mm. The maximum difference of elevation for the bottom and top sides is about 2.7 mm.

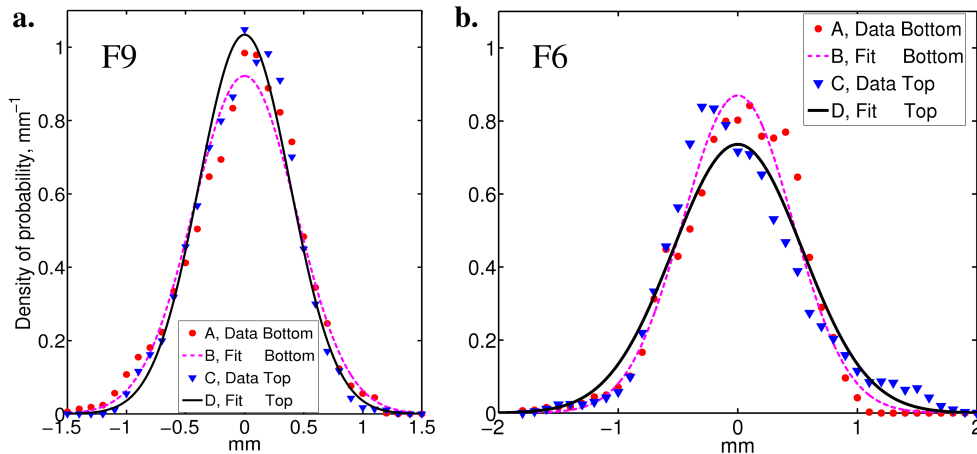


Figure 11: Probability density of the elevation of the bottom (A) and top (C) sides and their normal probability fits (B, D), for (a) F9 and F6 (b). For A, B, C, D, mean value is 0 mm and RMS is (a)  $0.4 \pm 0.05$  mm (b)  $0.5 \pm 0.05$  mm.

In order to compare potential anisotropy directions in the scaling laws of the top and bottom F9 surfaces, the surfaces are oriented relatively to one another (see details in paper 2). The autocorrelation function of the morphology elevation is computed (Fig. 11) for each side of F9 (see Marache et al. (2002) or Méheust and Schmittbuhl (2000, 2003) for comparable study on natural fractures). Estimates are done without taking into account major flaws along the external boundary of the core that are due to damage during coring. The autocorrelation  $C_2$  is computed in the real domain, and defined by the square root of the second moment of the elevation difference:

$$C_2(\vec{\Delta}) = \sqrt{\left\langle \left[ z(\vec{OM} + \vec{\Delta}) - z(\vec{OM}) \right]^2 \right\rangle}, \quad (1)$$

where  $z$  is the local elevation with respect to the mean plane,  $\vec{\Delta}(\Delta_x, \Delta_y)$  the lag vector (i.e. characteristic distance at which the correlation is computed), and  $\langle \rangle$  indicates that the average is computed over all the possible spatial points  $M$  so that  $z(\vec{OM})$  and  $z(\vec{OM} + \vec{\Delta})$  are defined. Self-affine properties of surfaces were tested by checking if (e.g. Barabàsi and Stanley (1995)):

$$C_2(\Delta) = C_2(\Delta_0) \left( \frac{\Delta}{\Delta_0} \right)^\zeta \quad (2)$$

is fulfilled, where  $\zeta$  is the Hurst exponent,  $\Delta_0$  is 1 mm and  $\Delta$  is the norm of  $\vec{\Delta}$ .

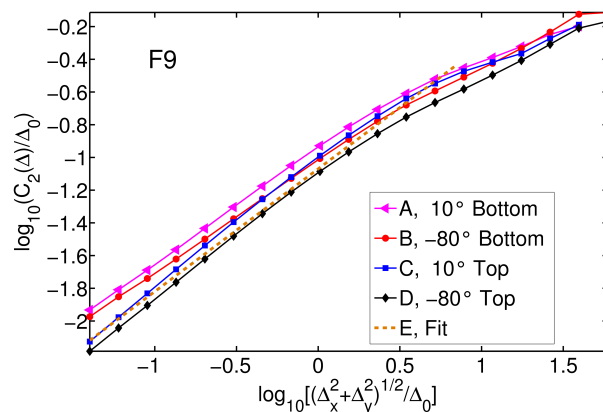


Figure 12: Plot of  $\log_{10} [C_2(\Delta)/\Delta_0]$  as a function of  $\log_{10} [\Delta/\Delta_0]$ , computed for discontinuity F9, in directions  $\theta$  equal to  $10^\circ$  and  $80^\circ$ , for the bottom side (A, B) and top side (C, D), respectively. Plot E is a linear fit  $\log_{10} [C_2(\Delta)/\Delta_0] = 0.75 \log_{10} [\Delta/\Delta_0] - 1.07$ , i.e.  $\zeta = 0.75$  and  $C_2(\Delta_0) = 0.09$  mm, plotted from  $\Delta = 40$   $\mu\text{m}$  to  $\Delta = 7$  mm.  $\Delta$  and  $C_2$  are in mm, and  $\Delta_0 = 1$  mm.

Figure 12 shows the 1D plot of  $\log_{10} [C_2(\Delta)/\Delta_0]$  as a function of  $\log_{10} [\Delta/\Delta_0]$  for two directions (hereafter demonstrated as being the directions showing the largest anisotropy):  $\theta = 10^\circ$ ,  $\theta = -80^\circ$ , where  $\theta$  is the angle between the  $x$ -axis and  $\vec{\Delta}$ . A linear trend has been fitted for lags ranging from 0.04 mm to 7 mm, for these directions. As the equation (2) translates into:

$$\log_{10} \left[ \frac{C_2(\Delta)}{\Delta_0} \right] = \zeta \log_{10} \left[ \frac{\Delta}{\Delta_0} \right] + \log_{10} \left[ \frac{C_2(\Delta_0)}{\Delta_0} \right], \quad (3)$$

the linearity of such a plot indicates that the surface is self-affine in the  $\theta$  direction, and  $\zeta$  and  $C_2(\Delta_0)$  can be deduced. In order to show the variability of  $\zeta$  and  $C_2(\Delta_0)$  as a function of  $\theta$ , a polar plot of both parameters is also shown (Fig. 13), where  $C_2(\Delta_0)$  is obtained from interpolation of  $C_2$  at 1 mm. The Hurst exponent computed so, slightly varies (amplitude of  $\pm 0.02$ ) around 0.69 (bottom side) or 0.74 (top side) according to the direction. The value  $C_2(\Delta_0)$  also regularly varies (amplitude of  $\pm 0.02$  mm) around 0.09 mm (top side) and 0.11 mm (bottom side), with extrema for  $\theta$  equals to  $10^\circ$  and  $-80^\circ$ .

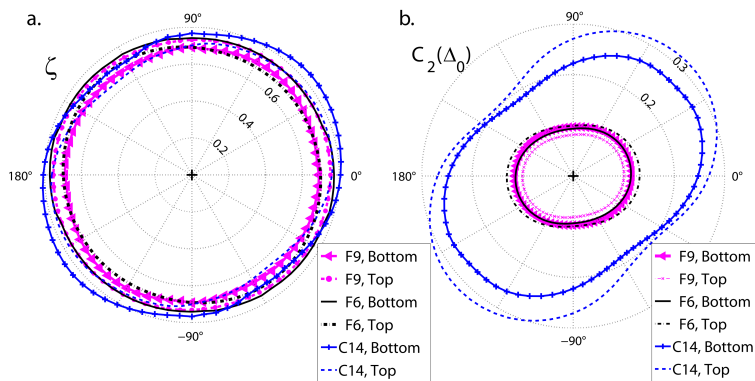


Figure 13: Polar plot of the Hurst exponent  $\zeta$  (a) and  $C_2(\Delta_0)$  in mm (b), as functions of  $\theta$  for the topography of the top and bottom sides, according to the angle, for the F9, F6 and C14 discontinuities as indicated by the labels. Note that the F6, F9 and C14 discontinuities are not oriented relatively to one another, on the contrary to each side relatively of a given pair.

The linearity of  $\log_{10}[C_2(\Delta)/\Delta_0]$  potentially does not fit over all the ranges of  $\Delta$ . In order to be able to observe possible multiple trends over various ranges of  $\Delta$ , a representation of  $\log_{10}[C_2(\Delta)/\Delta_0]$  as a function of the polar coordinates  $(\log_{10}(\Delta/l_p), \theta)$  (Ebner et al., 2010) is also shown (Fig 14), where  $l_p$  is 0.04 mm, i.e. the smallest pixel size used for topography measurement. If the surface is isotropic and self-affine over all the observed ranges, then the isovalue lines are a family of circles regularly distributed. An anisotropic self-affine surface would translate in a family of equally distributed and non circular isovalue lines. Fig 14a, computed for the topography of the bottom side of F9, shows that the variations of the Hurst exponent and  $C_2(\Delta_0)$  are of secondary order. A very similar figure was also obtained for the top side of F9. For both surfaces, the fit of the scaling laws can finally approximatively be done by  $\log_{10}[C_2(\Delta)/\Delta_0] = 0.75 \log_{10}[\Delta/\Delta_0] - 1.07$ , i.e.  $\zeta = 0.75$  and  $C_2(\Delta_0) = 0.09$  mm, from  $\Delta = 0.04$  mm to  $\Delta = 7$  mm.

Estimating the Hurst exponent with the  $C_2$  method requires a linear fit of equation (3). As the data contains inherent noise, the Hurst exponent deter-

mined therefore depends on the fitting method and, above all, on the chosen range of  $\Delta$  used to perform the fit. The  $C_2$  method might underestimate the Hurst exponent (Schmittbuhl et al., 1995b; Renard et al., 2006), but has the advantage of being easily applied in 2D on the whole natural surfaces. The study is in any case limited by the sample size and the sampling resolution.

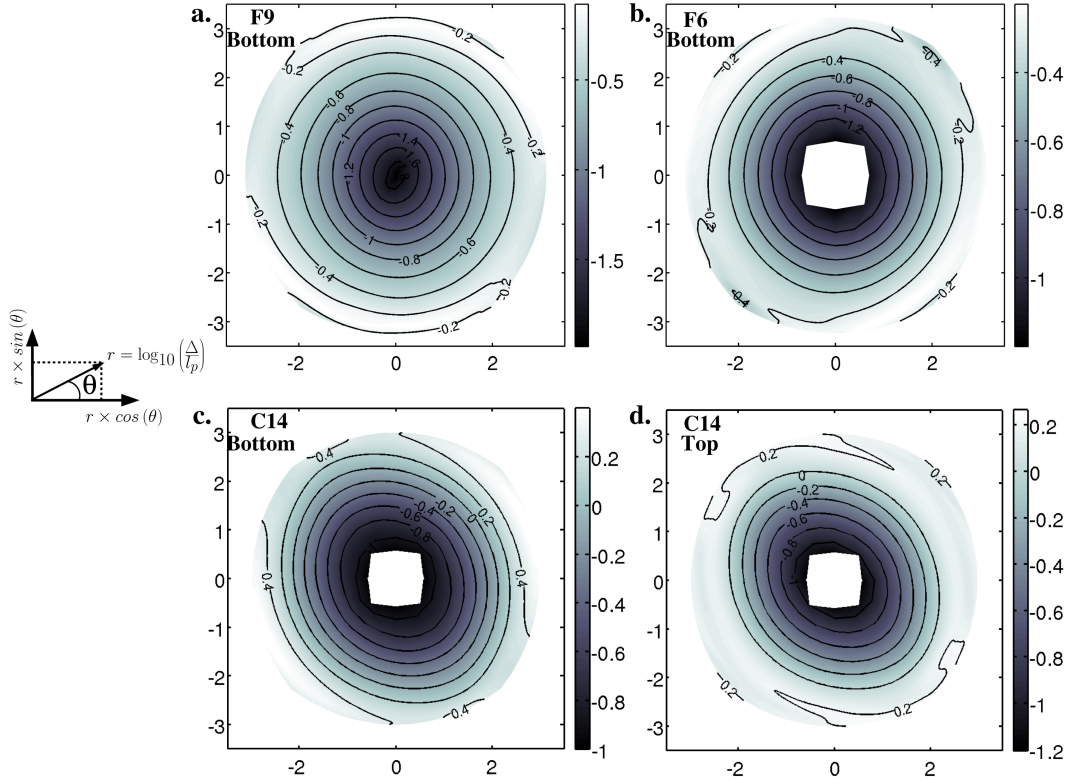


Figure 14: Representation of  $\log_{10}[C_2(\Delta)/\Delta_0]$  as a function of the polar coordinates  $(\log_{10}(\Delta/l_p), \theta)$ , where  $l_p$  is the pixel size used for topography measurement (0.04 mm), computed for the topography of the bottom side of F9 (a), F6 (b), C14 (c) and top side of C14 (d).  $\Delta$ ,  $C_2$  are in mm, and  $\Delta_0 = 1$  mm. At first order, the isovalue lines are families of circles approximately regularly distributed, showing that the surfaces are nearly isotropic and self-affine over all the observed ranges. At second order, C14 is slightly more anisotropic (especially the top one). Note that the range of isovalues is different between the surfaces, with higher  $C_2$  values for the C14 sides.

## 5.2 Statistical characterization of F6 discontinuity sides

The probability distribution function of the elevation was computed for both sides of F6 (Fig. 11b). Both probability distribution functions can be fitted with a normal probability density function having a standard deviation of  $0.5 \pm 0.05$  mm. This result shows that the elevation is slightly more variable than that of F9 sides which are less altered. The function  $\log_{10} [C_2(\Delta)/\Delta_0]$  as a function of  $\log_{10} [\Delta/\Delta_0]$  (Fig. 15) was also plotted for two directions corresponding to the directions  $\theta$  showing the largest anisotropy for each side. In fact, as for F9, the anisotropy of the bottom side of F6 is barely pronounced (figure 14b). A similar plot for the top side both has been made, showing that correlation of the top side is very similar to the bottom one. Both surfaces are also self-affine, from roughly 0.3 mm to 10 mm. The Hurst exponent computed for these ranges, regularly varies (amplitude of  $\pm 0.02$ ) around 0.70 (bottom side) or 0.76 (top side), according to the angle (Fig. 13a). The  $C_2(\Delta_0)$  value also regularly varies (by  $\pm 0.02$  mm) around 0.12 mm (top side) and 0.10 mm (bottom side) (Fig. 13b). Note that this scaling law is very close to that of the F9 sides, and as most observed fracture surfaces (Bouchaud, 1997).

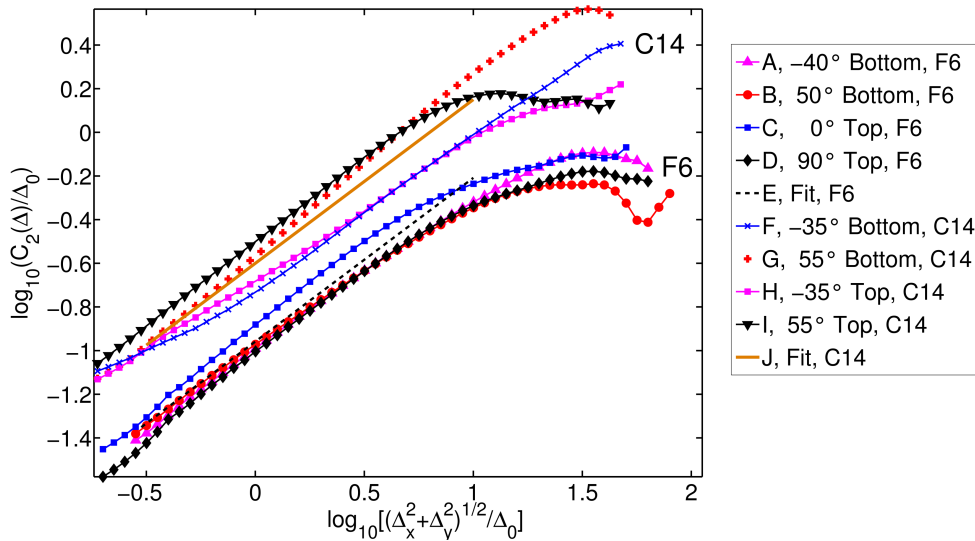


Figure 15: Plot of  $\log_{10} [C_2(\Delta)/\Delta_0]$  as a function of  $\log_{10} [\Delta/\Delta_0]$ , for the top and bottom sides of F6 (A, B, C, D) and C14 (F, G, H, I), for various directions  $\theta$ , as indicated by the labels. Plot E is the linear fit for F6 sides,  $\log_{10} [C_2(\Delta)/\Delta_0] = 0.75 \log_{10} [\Delta/\Delta_0] - 0.96$ , i.e.  $\zeta = 0.75$  and  $C_2(\Delta_0) = 0.11$  mm. Plot J is the linear fit for C14 sides,  $\log_{10} [C_2(\Delta)/\Delta_0] = 0.75 \log_{10} [\Delta/\Delta_0] - 0.6$ , i.e.  $\zeta = 0.75$  and  $C_2(\Delta_0) = 0.25$  mm.  $\Delta$  and  $C_2$  are in mm, and  $\Delta_0 = 1$  mm.

### 5.3 Statistical characterization of C14 discontinuity sides

$C_2$  was computed for the sides of discontinuity C14, and  $\log_{10} [C_2(\Delta)/\Delta_0]$  was plotted as a function of  $\log_{10} [\Delta/\Delta_0]$  for two directions  $\theta$  (Fig. 15). A linear trend can be observed from 0.3 mm to 10 mm, which means that a self-affine law can be fitted. As shown by figure 13, for both C14 surfaces,  $C_2$  is slightly anisotropic, with  $C_2(\Delta_0)$  values progressively varying according to the direction around 0.23 (by an amplitude of  $\pm 0.04$  mm) for the bottom side and around 0.26 (by an amplitude of  $\pm 0.06$  mm) for the top side, with extremal values around  $\theta$  equal to  $\pm 45^\circ$ . The Hurst exponent also shows an anisotropy, as it varies according to the direction (amplitude of  $\pm 0.06$ ) around 0.70 (top) and 0.76 (bottom). Note that the side measurements are relatively oriented to one another (see paper 2), so that the directions of anisotropy can be compared between both surfaces. The difference to an isotropic self-affine surface can be fully observed in Figs 14c and d which shows  $\log_{10} [C_2(\Delta)/\Delta_0]$  as a function of the polar coordinates  $(\log_{10}(\Delta/l_p), \theta)$  for both surfaces. It also shows that the anisotropy direction slightly evolves with the range of scales and that the range of  $C_2$  values is larger for the top surface than for the bottom one. By observing the rock sample, it was noticed that this anisotropy might correspond to a crystallization occurring along a preferential direction. If the anisotropy is considered as a second order effect, a rough common self-affine fit can be proposed with  $\zeta = 0.75$  (similarly to F9 and F6), and  $C_2(\Delta_0) = 0.25$  mm (more than twice higher than the value for F6 and F9).

## 6 Conclusion

A careful coring allowed us to study the surface morphology of the typical discontinuities present in the bedrock underlying the potential landslide zones near Draix (French Alps). Three sets of discontinuities have been distinguished: the fully open discontinuities, those filled by altered material and clay, and those sealed with calcite. Measurements with a laser profiler have provided statistical properties of the surface. It was observed that the probability density of the boundary elevation of the open (F9) and clay filled (F6) discontinuities is normal, with similar RMS for top and bottom sides. It was also shown that the surfaces of F6 and F9 are self-affine under a limited range, with little variation of the Hurst exponent and prefactor according to the direction for each pair of surfaces. The surfaces of the sealed discontinuity C14 were also shown to be self-affine, for a range of scale 0.3 mm to 1 cm, with visible variation of the Hurst exponent according to the direction. For each surface, the Hurst exponent range around  $0.75 \pm 0.05$ , which is of the same order than the one previously observed for various rocks (Power et al., 1987; Cox and Wang, 1993; Schmittbuhl et al., 1993, 1995a).

Such a multi-scaling property allows further modeling of transport properties (see paper 2). The measurement by X-ray computed tomography provided quantitative volumetric information, in particular about the thickness of the calcite-marl interface. The transition from calcite to marl density occurs in two steps: a sharp transition occurring on about 0.15 mm, followed by a smooth transition of several mm.

The authors would like to thank José Ortega for his help for the geological description of the core. We also thank Jean-Phillipe Malet and Alexandre Remaître for useful indications about Draix field observations, as well as Grégory Bièvre for helpful information about the SC1 drilling.

## References

- Antoine, P., Giraud, A., Meunier, M., and van Asch, T. (1995). Geological and geotechnical properties of the "Terres Noires" in southeastern France: Weathering, erosion, solid transport and instability. Engineering Geology, 40:223–234.
- Auradou, H., Drazer, G., Hulin, J. P., and Koplik, J. (2005). Permeability anisotropy induced by the shear displacement of rough fracture walls. Water Resources Research, 41(9):1–10.
- Barabási, A. L. and Stanley, H. E. (1995). Fractal Concepts in Surface Growth. Cambridge University Press, 2<sup>nd</sup> edition.
- Barton, C., Hickman, S., Morin, R., Zoback, M., Finkbeiner, T., Sass, J., and Benoit, D. (1997). Fracture permeability and its relationship to in-situ stress in the Dixie Valley, Nevada, Geothermal reservoir. In Twenty-Second Workshop on Geothermal Reservoir Engineering, volume SGP-TR-155, Stanford, California. Stanford University.
- Bondabou, K. (2007). Etude géologique et structurale d'un massif marneux fracturé sur le site expérimental de draix (Alpes du sud). Master's thesis, Département de l'Enseignement des Sciences de la Terre et de l'Environnement de Montpellier.
- Bouchaud, E. (1997). Scaling properties of cracks. Journal of Physics: Condensed Matter, 9:4319–4344.
- Brown, S. R. (1987). Fluid flow through rock joints: The effect of surface roughness. Journal of Geophysical Research, 92(B2):1337–1347.
- Carmichael, R. S. (1990). Practical Handbook of Rocks and Minerals. CRC Press Inc., U.S., 2<sup>nd</sup> edition.
- Cosandey, C., Mathys, N., Maquaire, O., and Esteves, M. (2007). Les marnes,

- roches imperméables? Processus générateurs des crues dans les marnes noires de la région de Digne les bains. In Actes des JSIRAUF, Hanoi.
- Cox, B. and Wang, J. (1993). Fractal surfaces: measurement and application in earth sciences. Fractal, 1(1):87–115.
- Cras, A. (2005). Etude et modélisation de la dynamique de fonctionnement hydrologique des bassins versants torrentiels marneux. Apport du traçage naturel. PhD thesis, Université d’Avignon et des Pays de Vaucluse.
- Drazer, G. and Koplik, J. (2002). Transport in rough self-affine fractures. Physical Review E, 66:026303.
- Ebner, M., Toussaint, R., Schmittbuhl, J., Koehn, D., and Bons, P. (2010). Anisotropic scaling of tectonic stylolites: a fossilized signature of the stress field? Journal of Geophysical Research. Article in Press.
- Fressard, M., Maquaire, O., Malet, J. P., Klotz, S., and Grandjean, G. (2009). Morpho-structure and triggering conditions of the Laval landslide developed in clay-shales, Draix catchment (South French Alps). In J. P. Malet, A. R. and Bogaard, T., editors, Landslide processes. From geomorphologic mapping to dynamic modelling., pages 111–114, France. CERG, Strasbourg.
- Garel, E., Marc, V., Emblanch, C., Debieche, T. H., Malet, J. P., and Klotz, S. (2009). Flow characterization in fractured black marls by single well pulse injection tests (Alpes-de-Haute-Provence, France). In J. P. Malet, A. R. and Bogaard, T., editors, Landslide processes. From geomorphologic mapping to dynamic modelling., pages 111–114, France. CERG, Strasbourg.
- Geoportail (2007–2009). <http://www.geoportail.fr>. ©2007–2009, IGN-BRGM Mentions légales Crédits.
- Glover, P. W. J., Matsuki, K., Hikima, R., and Hayashi, K. (1997). Fluid flow in fractally rough synthetic fractures. Geophysical Research Letters, 24(14):1803–1806.
- Hakami, E. and Larsson, E. (1996). Aperture Measurements and Flow Experiments on a Single Natural Fracture. International Journal of Rock Mechanics & Mining Sciences, 33(4):395–404.
- Iverson, R. M. and Reid, M. E. (1992). Gravity-driven groundwater flow and slope failure potential 1. Elastic effective-stress model. Water Resources Research, 28(3):925–938.
- Lofi, J., Pezard, P., Loggia, D., Garel, E., Gautier, S., Merry, C., and Bondabou, K. (2009). Petrophysical, borehole geophysics and geological characterization of tectonized clay shales drilled at Draix (southern French Alps).

- Hydrological Processes, Special issue, hydrology of clay shales and clayey sediments.
- Maquaire, O., Ritzenthaler, A., Fabre, D., Ambroise, B., Thiery, Y., Truchet, E., Malet, J.-P., and Monnet, J. (2002). Caractérisation des profils de formations superficielles par pénétrométrie dynamique à énergie variable : application aux marnes noires de Draix (Alpes-de-Haute-Provence, France). Characterisation of alteration profiles using dynamic penetrometry with variable energy. Application to weathered black marls, Draix (Alpes-de-Haute-Provence, France). Comptes Rendus Geosciences, 334(11):835 – 841.
- Marache, A., Riss, J., Gentier, S., and Chilès, J. P. (2002). Characterization and reconstruction of a rock fracture surface by geostatistics. International Journal for Numerical and Analytical Methods in Geomechanics, 26(9):873–896.
- Mathys, N. (2006). Analyse et modélisation à différentes échelles des mécanismes d'érosion et de transport de matériaux solides. Cas des petits bassins versants de montagne sur marne (Draix, Alpes-de-Hautes-Provence). PhD thesis, INP Grenoble.
- Méheust, Y. (2002). Écoulement dans les fractures ouvertes. PhD thesis, Université Paris Sud.
- Méheust, Y. and Schmittbuhl, J. (2000). Flow enhancement of a rough fracture. GRL, 27:2989–2992.
- Méheust, Y. and Schmittbuhl, J. (2003). Scale effects related to flow in rough fractures. Pure and Applied Geophysics, 160(5-6):1023–1050.
- Mery, C. (2008). Etude pétrographique et d'imagerie en forage d'un massif marneux fracturé sur le site expérimental de Draix. Master's thesis, Département de l'Enseignement des Sciences de la Terre et de l'Environnement de Montpellier.
- Neuville, A., Toussaint, R., and Schmittbuhl, J. (2009). Fracture aperture reconstruction and determination of hydrological properties: a case study at Draix (French Alps). Hydrological Processes, Special issue, hydrology of clay shales and clayey sediments. Submitted, in revision.
- Noiriel, C. (2005). Contribution à la détermination expérimentale et à la modélisation des différents processus contrôlant l'évolution géochimique, structurale et hydrodynamique des roches fissurées carbonatées. PhD thesis, École des Mines de Paris.
- Plouraboué, F., Kurowski, P., Boffa, J. M., Hulin, J. P., and Roux, S. (2000). Experimental study of the transport properties of rough self-affine fractures. Journal of Contaminant Hydrology, 46:295–318.

- Power, W., Tullis, T., Brown, S., Boitnott, G., and Scholz, C. (1987). Roughness of natural fault surfaces. Geophysical Research Letters, 14(1):29–32.
- Renard, F., Voisin, C., Marsan, D., and Schmittbuhl, J. (2006). High resolution 3d laser scanner measurements of a strike-slip quantify its morphological anisotropy at all scales. Geophysical Research Letters, 33(4).
- Schmittbuhl, J., Gentier, S., and Roux, S. (1993). Field measurements of the roughness of fault surfaces. Geophysical Research Letters, 20(8):639–641.
- Schmittbuhl, J., Schmitt, F., and Scholz, C. (1995a). Scaling invariance of crack surfaces. Journal of Geophysical Research, 100(B4):5953–5973.
- Schmittbuhl, J., Steyer, A., Jouniaux, L., and Toussaint, R. (2008). Fracture morphology and viscous transport. International Journal of Rock Mechanics & Mining Sciences, 45:422–430.
- Schmittbuhl, J., Vilotte, J., and Roux, S. (1995b). Reliability of self-affine measurements. Physical Review E, 51:131–147.
- Terzaghi, K. (1936). The shearing resistance of saturated soils and the angle between the planes of shear. In Proceedings, 1st International Conference on Soil Mechanics and Foundation Engineering, volume 1, pages 54–56, Cambridge, USA.
- Vicente Silvestre, M. V., Ribeiro e Sousa, L., and Hack, R. (2002). Laboratory study of geomechanical and hydro-mechanical characterisation of discontinuities. News Journal International Society for Rock Mechanics (ISRM), 7(2):9–15.
- Wyllie, D. C. (1999). Foundations on rock. Spon Press, London, U.K., 2<sup>nd</sup> edition.
- Yamakoshi, T., Mathys, N., and Kiotz, S. (2009). Time-lapse video observation of erosion processes on the Black Marls badlands in the Southern Alps, France. Earth Surface Processes and Landforms, 34(2):314–318.
- Zhang, S., Lai, Y., Zhang, X., Pu, Y., and Yu, W. (2004). Study on the damage propagation of surrounding rock from a cold-region tunnel under freeze-thaw cycle condition. Tunnelling and Underground Space Technology, 19:295–302.